International Journal of Heat and Mass Transfer 223 (2024) 125263



Contents lists available at ScienceDirect

International Journal of Heat and Mass Transfer

journal homepage: www.elsevier.com/locate/ijhmt





Micro-scaling numerical model coupled with experimental validation of the pressure drop for dense wire mesh

Daniel Sanchez-Señoran [a,b], Miguel A. Reyes-Belmonte [b], Meryem Farchado [a], Antonio L. Avila-Marin [a,*]

[a] CIEMAT, Plataforma Solar de Almeria, Avda. Complutense, 40, Madrid, E-28040, Spain
[b] Rey Juan Carlos University, Chemical, Energy and Mechanical Technology, C/Tulipán, s/n, Móstoles, Madrid, E-28933, Spain

ARTICLE INFO

Keywords:
Volumetric absorbers
Volumetric receivers
Numerical methodology
Differential Pressure
Central Receiver System
Experimental Validation

ABSTRACT

In central receiver systems, differences in designs and performances between open volumetric receivers have been established over the years, with a primary focus on the convective heat transfer coefficient. However, the other main parameter, the differential pressure, has not been thoroughly studied despite its significance. For that reason, in this research, the pressure drop is evaluated for dense wire meshes. In all the studies, a sensitivity analysis is conducted maintaining the temperature of the absorber at 300 K and varying the inlet velocity from 0.5 to 5 m/s. Darcy's law with the Forchheimer extension is employed in this work to estimate the differential pressure and obtained the individual correlations.

Firstly, in order to understand the change in the pressure of a fluid that has passed through dense wire meshes used as volumetric receivers, a detailed CFD methodology is used to estimate the differential pressure compared to the experimental tests. The pressure drop correlation of the CFD methodology yields a maximum and average deviation with respect to the experimental tests of 3.6% and 1.2% respectively.

Secondly, three individual correlations are established for the three wire diameters studied, 0.1, 0.4, and 0.7 mm. For wire diameters ranging from 0.1 to 0.7 mm with a fixed 80% single mesh porosity and staggered stack pattern in dense wire meshes, a generalised correlation based on the Ergun equation is developed. The generalised correlation shows a maximum deviation of up to 4.1% and an average deviation of up to 2.5% when compared to the CFD values obtained with the methodology developed.

Introduction

Starting in the last century, porous media have been introduced in several fields, from nuclear to hydrogen energy, in addition to other disparate applications. In that period of time, porous media have been studied with different materials and geometries as both geometrical parameters and the materials themselves affect behaviour and can be adapted.

In concentrated solar tower (CST) applications, the porous medium is in the receiver to which the heliostat directs the sun's rays. A fluid flowing through the porous medium absorbs heat to be used in electricity generation and other processes. In this application, the use of porous materials in open volumetric receivers (OVRs) can provide advantages. First, higher operational temperatures can be achieved than with the tubular receivers currently being used. Second, simpler receivers can be built as the working fluid, air, just has to flow through the porous medium. And, third, the receiver's simplicity reduces costs as well. The porous medium materials studied in CST are ceramics and metals [1–6], and the choice is made based on the operational temperature desired for the receiver. OVRs have two main parameters which are the convective heat transfer coefficient (HTC) and the differential pressure or pressure drop, which are affected by the geometrical parameters of the porous medium. As the pressure drop and HTC are the two main variables, analysing both are key to optimising and improving the fluid dynamic and thermal performance of volumetric receivers. Thus both variables have been analysed in relation to the geometrical parameters of the volumetric absorber, regardless of material [7].

Differential pressure in fluids passing through matrices is a parameter which had been studied for many years. In 1956, L. S. Tong and A. L. London [8] presented an experimental analysis of flow friction and heat transfer for the nuclear industry over two matrices, crossed-rod and woven-screen. Years later, in 1960, A. L. London et al. [9] presented a flow friction and an experimental study of the heat transfer

* Corresponding author.
E-mail address: antonio.avila@ciemat.es (A.L. Avila-Marin).

https://doi.org/10.1016/j.ijheatmasstransfer.2024.125263
Received 15 October 2023; Received in revised form 15 January 2024; Accepted 29 January 2024
Available online 7 February 2024
0017-9310/© 2024 The Author(s). Published by Elsevier Ltd. This is an open access article under the CC BY-NC-ND license (http://creativecommons.org/licenses/by-nc-nd/4.0/).

Nomenclature

M	Mesh count, mm^{-1}
d	Wire diameter, mm
w	Wire spacing, mm
c_f	Compactness factor
N	Number of meshes of the mesh stack
t	Thickness of the mesh stack, mm
$\varnothing_{SM}$	Single mesh porosity, %
$\varnothing_{ST}$	Staggered mesh porosity, %
C	Unit cell mesh constant
a_v	Specific surface, m^{-1}
d_h	Hydraulic diameter, m^{-1}
ρ	Density, kg m^{-3}
$\boldsymbol{V}$	Superficial velocity, m s^{-1}
μ	Dynamic viscosity, kg m^{-1} s^{-1}
$\vec{v}$	Interstitial velocity, m s^{-1}
K_1	Viscosity coefficient, m^2
K_2	Inertial coefficient, m
TA	Thermal anemometer
deltaP	Differential pressure meter
E	Experimental
N	Numerical
CFD	Computational Fluid Dinamycs
IC	Individual Correlation
GC	Generalised Correlation
D	Deviation

characteristics of crossed-rod matrices for a porosity ranging from 0.5 to 0.83 that was considered for different applications. Then in 1969, Beavers and Sparrow [10] studied the characteristics of a wide range of flow velocities on latticeworks of metallic fibres through experimentation. This study concluded with a correlation based on a non-Darcy flow in porous media for newer technologies at that time.

Later, in a 1994 study, Du Plessis et al. [11] worked on a pressure drop study for the chemical field using an analytical foam structure model, based on a rectangular representative unit cell (RUC) concept, and validated with an experimental program at low flow velocities, for glycerol and water as working fluids in three metallic foams. Those metallic foams had a porosity ranging from 0.973 to 0.978, but the real difference was in the pore diameters which ranged from 0.25 to 0.87 mm. This work concluded with a comparison to a capillary model, in order to present the RUC concept as being capable of predicting the pressure drop for both Darcy and non-Darcy flows. Bhattacharya et al. [12], in 2002, worked with different metal foam samples with high porosity, from 0.905 to 0.978. Those metal foams were analysed mathematically and tested experimentally to determine the conductivity and the differential pressure coefficients. Analytical models were proposed to determine the differential pressure coefficients, and the correlations presented were based on the correlations in Du Plessis [11] work.

New metal foams for other industrial fields were studied by Khayargoli et al. [13] in 2004. His experimental study concluded that the pressure drop of these new metal foams can be predicted with the Ergun equation, as presented in Tadrist et al. [14], together with the calculation of the constants. Khayargoli used nickel-chromium metal foams with a range of pore sizes from 11 to 53 PPI and thickness from 5 to 13 mm. In 2008, Jean-Philippe Bonnet et al. [15] studied experimental pressure drops for metal foams with two working fluids, air with a maximum velocity flow of 20 m/s and water with a maximum velocity flow of 0.1 m/s. In this study, the pressure drop parameters were correlated with the pore size. In order to obtain those results, Bonnet evaluated samples based on nickel, nickel-chromium and copper with porosity ranges from 0.87 to 0.94, with fixed dimensions of 50 mm x 150 mm and a thickness ranging from 1.5 to 10.3 mm depending on pore size.

Focusing on wire mesh structures, in 2009, Joo et al. [16] studied the pressure drop characteristics of a woven wire bulk Kagome structure (WBK) for application in heat dissipaters using two different orientations. Joo concluded that WBK can dissipate heat with a lower pressure drop than other heat dissipation media. For catalytic reactors, in that same year, Kolodziej and Lojewska [17] studied the flow resistance of wire gauzes, three woven and knitted gauzes with a wire diameter ranging from 0.0977 to 0.3 mm and a porosity ranging from 0.673 to 0.967. They concluded proposing a new analytical model based on the Ergun equation.

In heat exchange applications, in 2010, Dyga et al. [18] presented a pressure drop and heat transfer coefficient study of wire mesh packing with both air and water as working fluids. Dyga used a packing with a wire mesh size of 1.3 mm and a wire diameter of 0.25 mm with a porosity of 0.764, obtaining promising results in heat exchange when air was used as the working fluid.

In 2016, Ma et al. [19] carried out experimental tests of woven wire meshes (Dutch weave) with a wire diameter of 0.14 mm and porosities ranging from 0.256 to 0.551. In this study Ma built woven wire meshes combining two homogenous porosities, each 3 mm thick, in a pack. Ma showed that the pressure drop and the inertia parameter increase with the decrease in porosity, whereas the permeability parameter presents the opposite behaviour. Other authors that have worked with metallic wire meshes, in this case for vertical channel applications are, in 2016, Kurian et al. [20] and, in 2019, Kotresha et al. [21]. The studies were based on an experimental and a local thermal non-equilibrium (LTNE) numerical model respectively, in which the pressure drop and the heat transfer of three brass wire mesh blocks were presented with their respective correlations. In Kurian's experimental work, the inlet air velocity range was from 0 to 2 m/s, with power inputs to the heater of 20, 40 and 60 W. In Kotresha's LTNE model the simulated air velocities were from 0.05 to 2.5 m/s, and the simulation of the brass wire mesh was considered laminar for having a Reynolds number lower than 150, whereas for the channel and the non-porous region, k-kl-ω transient and k-ω models were assumed respectively. In both the Kurian and Kotresha studies the three brass wire mesh blocks had porosities of 0.77, 0.81 and 0.85. On 2021, Zhao et al. [22] reviewed the literature on pressure drop for porous structures and concluded that open cell foam pressure drops are determined by porosity and pore diameter. However, he could offer no general correlation for predicting the drops because the morphological characteristics of foams cannot be determined accurately due to the irregular structure, unlike lattice frame structures, woven wire structures and structured packed beds whose regular structures do permit accurate determination of their morphological characteristics.

In concentrated solar power technology, it is possible to find pressure drop studies, such as in the Stirling engine generator field in which authors like Thomas et al. [23], in 2000, studied the differential pressure and heat transfer of wire screens and metal felts experimentally. In this work the characteristics of the wire screens studied were a wire diameter ranging from 0.0533 to 0.094 mm and a porosity ranging from 0.6232 to 0.781, for the studied metal felts, the wire diameters ranged from 0.0127 to 0.0508 mm, with porosities ranging from 0.688 to 0.8405. Thomas concluded with correlations for both the pressure drop and heat transfer.

In concentrated solar tower (CST) field, Becker et al. [24] in 2006, developed a numerical model to predict the flow instabilities produced by high radiation in porous materials applied to OVR. Becker emphasised the properties that are needed for LTNE pressure drop numerical studies.

In 2013, Costa et al. [25] presented a numerical study of the pressure drop in a wound woven wire matrix in the Stirling engine generator field. In this work, two configurations were studied, one aligned and the other non-aligned, with different porosities ranging from 0.387 to 0.641. Costa concluded with a general correlation and two specific correlations of the pressure drop for the configurations studied. Also, in 2021, York et al. [26] evaluated the influence of offset alignment and spacing on the pressure drop in wire mesh through a 3D CFD approach. Three cases were presented, first one where the wire meshes were aligned to each other keeping the wires parallel, a second case where the mesh layers were offset from one to another by 45°, and a third case where the wire meshes were randomly stacked. The porosity of the wire mesh stack was 0.66 and its hydraulic diameter was 0.213 mm. The study concluded by presenting a new correlation for calculating the pressure drop accurately, although the pressure losses in wire mesh stacks can be predicted better with no spacing than with spacing. And, recently, in concentrated solar tower (CST) field, Broeske et al. [27] developed a numerical methodology to study flow instabilities in 3D-shaped honeycomb absorbers.

This review shows that the literature on dense wire meshes for concentrated solar tower applications primarily focuses on the convective heat transfer coefficient (HTC) and does not delve into evaluating pressure drop as thoroughly as for foams [28–33]. Despite the importance of differential pressure in determining the hydrodynamic behaviour and the power consumption needed in CST plants using OVR technology with air as the heat transfer fluid. As a result, the authors have developed a computational fluid dynamic (CFD) methodology that has been validated with experimental data to address this gap in the literature. The CFD methodology has been used to establish individual correlations for each case studied using Darcy's law with the Forchheimer extension. A comparison between each case has been carried out in order to capture the different behaviours when geometrical parameters are modified. And, to conclude, for staggered patterns in dense wire meshes with a 80% single mesh porosity, a general correlation has been developed using the Ergun equation, which takes into account the geometrical parameters, to implement in OVR optimisations.

Description of the lattice structure

Plain weave wire meshes following a staggered stack pattern are the object of this work. Fig. 1 shows two views of the plain weave screen cell units used in dense wire meshes, where the main geometrical parameters are the wire diameter (d), the wire spacing or pitch (w), and the mesh count ($M = (d + w)^{-1}$). Moreover, Fig. 2 depicts the staggered

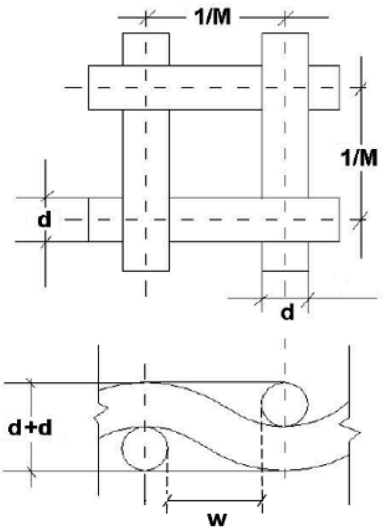


Fig. 1. Plain-weave square single mesh [34].

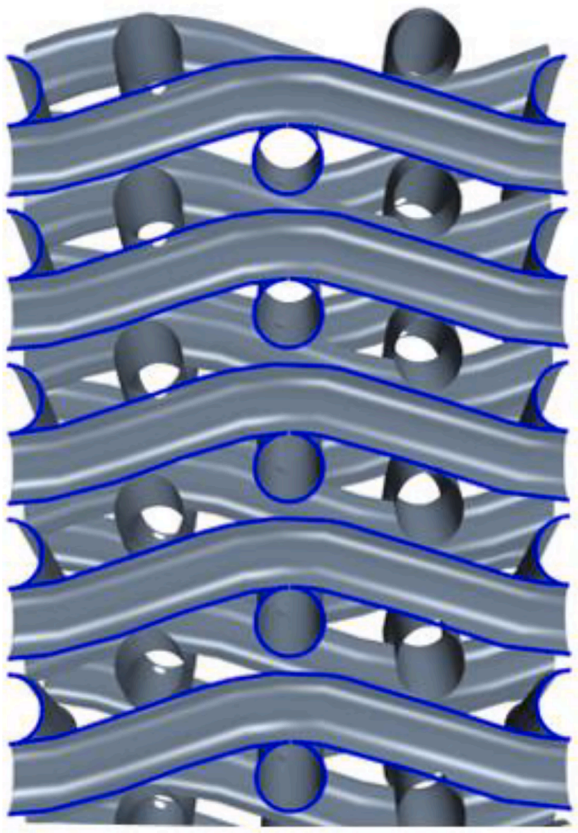


Fig. 2. Staggered stack pattern used in the cases analysed. The odd meshes are highlighted.

stack arrangement, following a dense pattern, as adopted in this study [34,35]. Here odd meshes (outlined in blue) have the same orientation but are shifted in the z-direction, while even meshes, besides being shifted in z-direction, are also offset in x- and y-directions by a value of $0.5 \cdot M^{-1}$ from the odd ones.

The geometrical parameters that define the staggered pattern are the same ones as for the plain weave screen cell unit, d, w and M, together with the compactness factor (c_f) describing the degree of compactness in the dense pattern. Based on these geometrical parameters, distinct properties of the wire mesh geometry can be defined using the porosity ($\varnothing$), specific surface (a_v) and hydraulic diameter (d_h). These geometrical properties, which are defined in the literature [18,36,37], influence the thermal and hydrodynamic behavior of the dense wire meshes [38] following the next expressions:

$$\varnothing = 1 - \frac{\pi \cdot M \cdot d}{4 \cdot c_f} \cdot C \tag{1}$$

$$a_v \cdot d = \frac{\pi \cdot M \cdot d}{c_f} \cdot C \tag{2}$$

$$d_h = \frac{4 \cdot \varnothing}{a_v} \tag{3}$$

Where c_f is the compactness factor, and is defined as $c_f = t/(N(2 \cdot d))$. For an uncompressed or inline wire mesh stack the c_f value is 1, elsewhere the c_f value is lower than 1. Also, t is the thickness of the absorber and N is the number of meshes. Parameter C is a constant and dimensionless value that depends on the geometrical properties "M·d" of the main cell unit.

$$C = \left(\frac{M \cdot d}{2} + \frac{1}{2 \cdot M \cdot d}\right) \arcsin\left(\frac{1}{\frac{M \cdot d}{2} + \frac{1}{2 \cdot M \cdot d}}\right) \quad (4)$$

Cases studied

This work uses a numerical methodology, with experimental validation, to estimate the differential pressure in dense wire meshes, plus a numerical study of how geometrical parameters, M and d, influence the pressure drop of wire meshes in a staggered arrangement with the same porosity.

Table 1 summarises the main geometrical parameters and properties used in this work for the section where the numerical methodology is presented and validated (section 5.1), and for the section where the influence of the geometrical parameters is evaluated (section 5.2). All the cases follow a staggered stack arrangement as shown in Fig. 2.

For the validation in section 5.1, a wire mesh with 1 mm diameter, 0.2 mm^{-1} mesh count, 83.9% single wire mesh porosity, and 70% dense wire mesh porosity with staggered stack has been used. Those parameters and properties for the wire mesh were chosen in order to use material left over from previous experimental research in the validation [5, 38,39].

Section 5.2 deals with the influence of geometrical parameters d and M on the pressure drop in a dense wire mesh structure. To do this, three wire meshes with three distinct diameters, 0.1 mm, 0.4 mm and 0.7 mm, all having a single mesh porosity of 80%, and a staggered mesh porosity of 64%, have been studied.

Methodologies for predicting differential pressure

As mentioned in the introduction, there are a great number of articles dealing with the pressure drop in many types of porous media. However, there is a dearth of literature on the pressure drop for dense wire meshes with a staggered pattern for CSP applications, particularly as regards describing a numerical methodology, validating it experimentally and presenting correlations of the influence of the geometrical parameters. This section presents the numerical methodology implemented using the computational fluid dynamics (CFD) software STAR-CCM+, as well as an experimental methodology for studying the pressure drop in staggered stack wire meshes.

Numerical methodology

Porous media shape

For the CFD analysis, two different geometrical shapes with a dense staggered stack pattern have been adopted which are presented in Fig. 3:

a) Geometry 1 (G1), Fig. 3 left, depicts a detailed representative geometry based on a rectangular shape. This geometry has usually been adopted for the numerical study of the convective heat transfer coefficient of wire meshes at high temperatures [40].
b) Geometry 2 (G2), Fig. 3 right, shows a representative geometry based on a circular shape, which was adopted for the experimental study of porous structures [41,42].

Note that the inlet area of G2 is larger than the inlet area of G1, which makes G2 more representative of the size of the real samples.

Governing equations and assumptions

The detailed or micro-scaled simulation employed in this work is the most accurate modelling technique in which real 3D geometry can be represented. The physics equations that govern the fluid flow through the staggered stack wire mesh medium are [43–45]:

1) Continuity equation

$$\nabla(\rho \cdot \vec{v}) = 0 \quad (5)$$

2) Momentum equation

$$\nabla(\rho \cdot \vec{v} x \vec{v}) = \nabla\sigma + f_b \quad (6)$$

Where ρ is the density of the fluid, σ is the stress tensor, f_b is the resultant of the body forces and $\vec{v}$ is the velocity of the fluid.

In every simulation, the conservation equations need some assumptions and boundary conditions to be solved at all. The main assumptions adopted here are:

a) The 3D model is based on steady state simulations.
b) The fluid is air with constant physical properties evaluated at 300 K.
c) The segregated flow solver is implemented based on a second order convection equation.
d) Simulations are carried out considering laminar flow.

In order to select the flow regime in the simulation correctly, laminar and turbulence fluid flow regimes were compared for geometries 1 and 2 (Fig. 3). Table 2 depicts the pressure drop for geometries 1 (G1) and 2 (G2) with laminar and turbulence fluid flow and their deviations. For this analysis, the highest inlet air velocity studied, 5 m/s, has been used with a temperature of 300 K, considering the wall boundaries as symmetry planes (section 4.1.3). The results show that the maximum pressure drop deviation between the two regimes is around 8% and 5% for G1 and G2 respectively, which means that either regime will yield equally accurate results in this context. Moreover, the validation section (section 5.1) confirms these results.

Boundary conditions and mesh generation

A precise definition of the boundaries in the numerical model is required and determines the accuracy of the convergence, as well as the feasibility of solving the physical problem. The main boundaries are presented in Fig. 4 for geometry G2. It mainly consists of:

a) Inlet surface boundary: a constant velocity at the inlet surface of the configuration was adopted, with a static temperature of 300 K. 6 velocities between 0.5 and 5 m/s were used in the parametric study.
b) Outlet surface boundary: a pressure outlet of 0 Pa was defined.
c) Interior wire surface: all the wires of the meshes are considered as non-slip walls.
d) Lateral surface boundary: the lateral side of each configuration has two possible boundary conditions, a wall or a symmetry plane. When

Table 1
Geometrical properties and parameters of the volumetric absorbers studied in the experimental validation and numerical simulations.

Case	Case Number	d, mm	M, mm^{-1}	$\varnothing_{SM}$, %	$\varnothing_{ST}$, %	a_v, m^{-1}	cf, -
Experimental validation	# 0	1.0	0.20	83.9	70.1	1,194	0.58-0.7*
Numerical simulation	# 1	0.7	0.35	80.0	64.4	2,031	0.56
	# 2	0.4	0.61		64.4	3,548	0.57
	# 3	0.1	2.44		63.7	14,001	0.58

*c_f value varies with the number of meshes in the absorber.

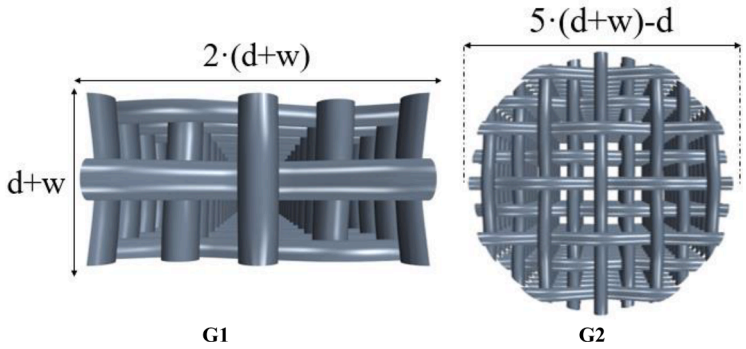


Fig. 3. Geometries studied for pressure drop: (G1) Rectangular and (G2) Circular.

Table 2
Pressure drop as a function of the fluid flow regime for geometries 1 and 2.

Geometry	Laminar flow, Pa	Turbulence flow, Pa	Deviation, %
G1	591	543	8.1
G2	141	149	5.2

a wall boundary condition is selected, an impenetrable surface is imposed on the lateral surface. In addition, for this particular case, the fluid velocity is zero when it sticks to the wall, which is known as no-slip wall condition. However, the symmetry plane boundary reduces the extent of the computational domain by mirroring the geometry and the flow in certain locations. In this case, the option of using symmetry plane boundary makes sense because a representative geometry is used [43,44].

In this study, and in order to develop the most accurate CFD methodology to predict the pressure drop through the porous media, two different boundary conditions, wall and symmetry plane, have been evaluated for each geometry (G1 & G2). As a result, two different simulations were performed for geometries G1 & G2, and are compared to experimental data.

Table 3 summarises the four cases studied with their respective boundary conditions and the number of cells implemented in the CFD software.

Assessing the intricate phenomenon of how air moves through various dense wire mesh configurations is challenging, as a result it is important to use high-quality meshes. In this research, the cases analysed have been discretised using polyhedral cells for the fluid domain and prism layers in the wire-air interface to capture the resistance of the porous media to the fluid flow. Appendix 1 presents further information about the sensitivity grid analysis. Fig. 4 shows a free space behind each geometry that was left to avoid flow recirculation issues while Fig. 5 depicts the mesh for both configurations.

Experimental methodology

Experimental lattices

For the analysis and validation of the numerical methodology, three bespoke wire mesh configurations with staggered arrangement were made (Fig. 6) to measure the pressure drop experimentally. Three different lattices with a diameter of 60 mm were used to verify the numerical results. The lattices have a wire diameter of 1 mm, a mesh count of 0.2 mm^{-1} and a porosity of 70.1%. The three lattices used had 5, 10 and 15 meshes, which accounts for a thickness of 7, 11.7 and 17.2 mm respectively.

Experimental setup

To measure the pressure drop of the bespoke lattices, an experimental setup was used. Fig. 7 depicts that setup, which consists of the

Table 3
Boundary conditions of each geometry studied.

Geometry	Lateral surface	Arrangement	Number of Cells
1 – Rectangular	Symmetry Plane	A1	3,024,815
1 – Rectangular	Wall	A2	3,352,799
2 – Circular	Symmetry Plane	A3	8,002,499
2 - Circular	Wall	A4	8,893,365

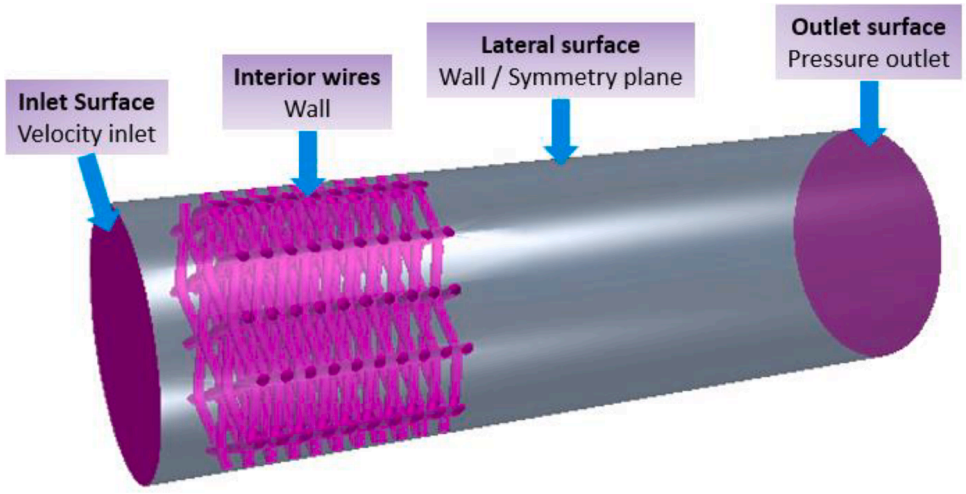


Fig. 4. Boundary conditions adopted in the CFD numerical simulations.

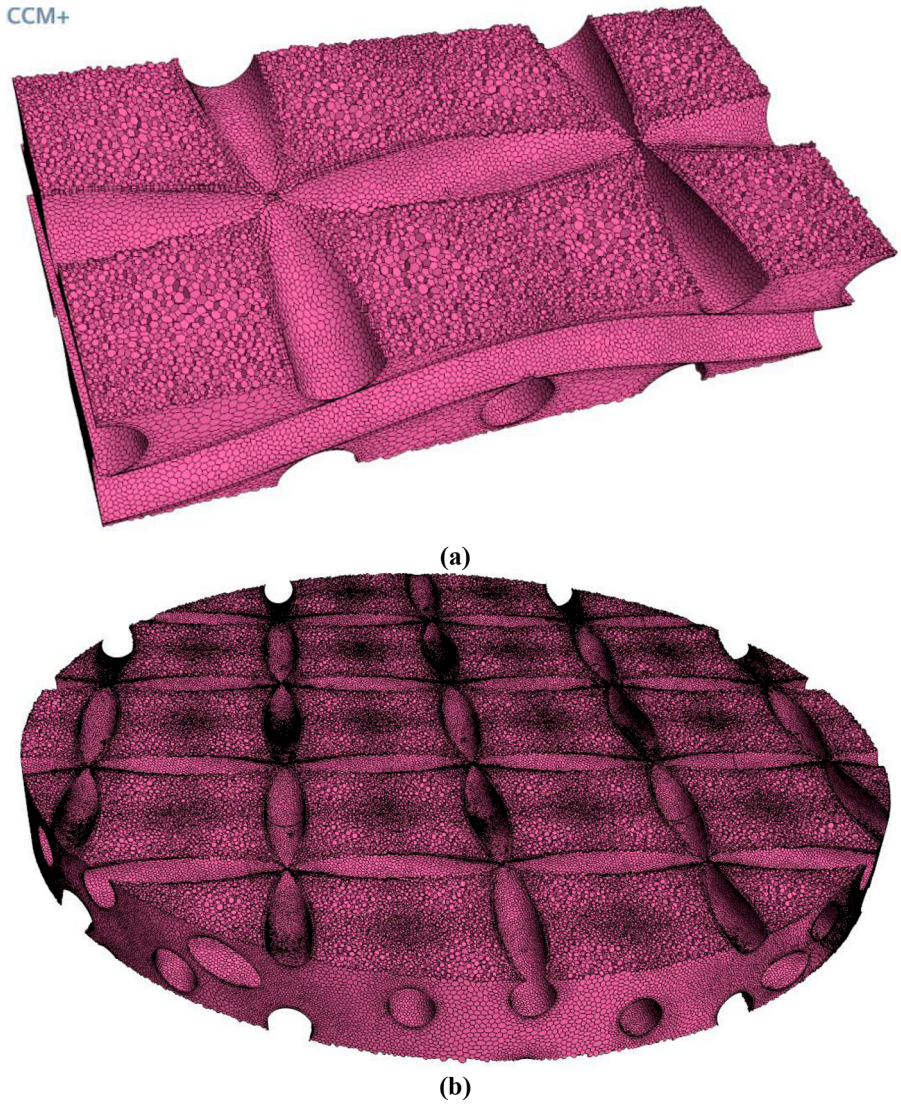


Fig. 5. Detailed threshold grid for: a) geometry 1, and b) geometry 2.

following components:

1. Blower: It is capable of producing the air inlet velocities between 0.5 and 5 m/s.
2. Valve: The main purpose of the flow control valve is to adjust the mass flow rate.
3. Anemometer: It measures the air velocity and the air temperature. The thermal anemometer is an Airflow TA430 with an air velocity accuracy of 0.01 m/s, a flow rate accuracy of 0.01 m^3/s and a temperature accuracy of 0.1 K.
4. Pressure drop meter: The differential pressure meter has a range of 0 to 130 mbar, and is accurate to 0.01 mbar. The lattice is placed in a holder with inlets on each side to measure the pressure drop.

The typical experimental procedure involves, firstly, placing the 60 mm diameter porous sample in the sample holder, secondly, connecting the blower after fully opening the control valve, then, turning on the anemometer and the differential pressure meter to start the process. The measurement of each sample took about one hour. During this time, the flow control valve was regulated to achieve six different air velocities, ranging from 0.5 to 5 m/s. At the beginning, the valve was opened to have the maximum air velocity (~5 m/s), after each velocity step all the components were kept constant until a steady state and a fully developed fluid flow was achieved, usually 10-15 minutes. After the six steps, the lowest air velocity was achieved (~0.5 m/s). Each porous sample was tested three times to demonstrate the general repeatability of the procedure.

In the experimental setup, all elements are placed at sufficient distances from each other to achieve a fully developed flow under any air velocity condition. Furthermore, the results from the thermal anemometer and the differential pressure meter have been doubled-checked with another pair of meters as can be seen in Appendix 2.

Discussion and Results

This section includes, firstly, the validation of the numerical methodology presented in section 4.1, with the experimental tests for case # 0 (Table 1). Secondly, it presents the numerical methodology employed to analyse the influence of the geometrical parameters over the pressure drop for a fixed porosity, cases # 1, # 2 and # 3 (Table 1).

Both, experimental and numerical results are based on a parametric study with the superficial inlet velocity of the air ranging from 0.5 to 5 m/s, at an air constant temperature of 300 K. The correlations for each case are defined by Darcy's law with the Forchheimer extension [46]:

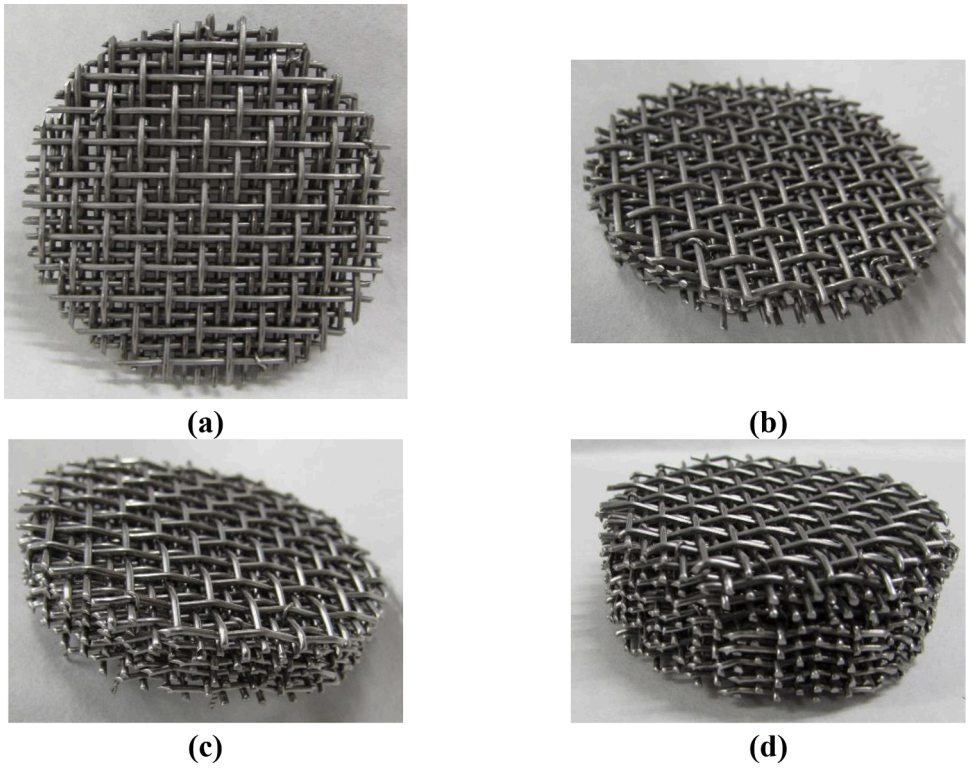


Fig. 6. Bespoke lattices. (a) Front surface of lattice 1, (b) Profile of lattice 1, (c) Profile of lattice 2, (d) Profile of lattice 3.

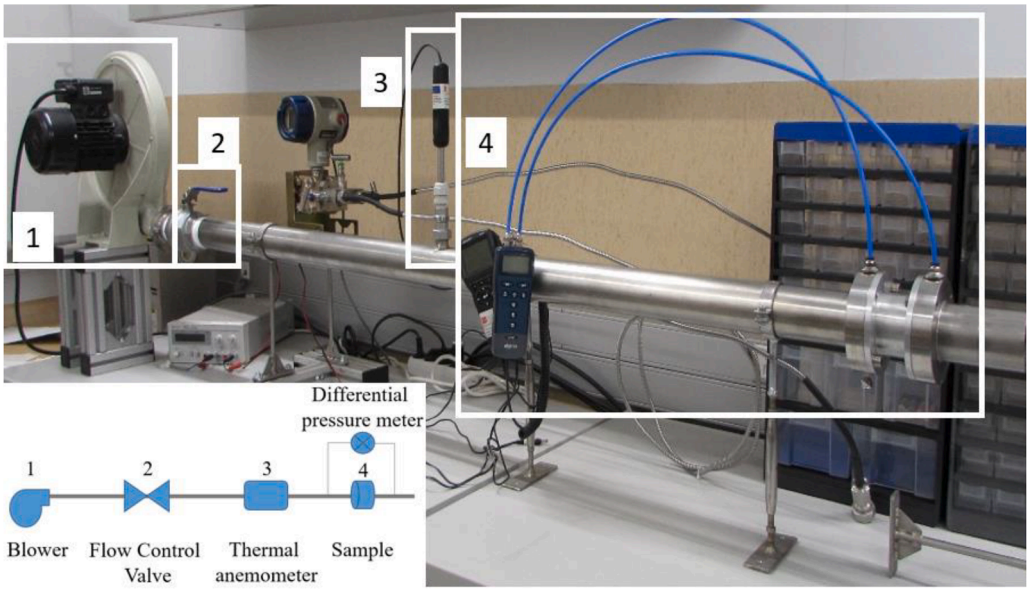


Fig. 7. Experimental setup to measure the differential pressure in porous samples. (1) Blower, (2) flow control valve, (3) thermal anemometer and (4) differential pressure meter and the sample holder.

$$-\frac{dp}{dz} = \frac{\mu}{K_1}V + \frac{\rho}{K_2}V^2 \tag{7}$$

where V is the superficial velocity, μ is the dynamical viscosity of the fluid at 300 K, ρ is density of the fluid at 300 K, and K_1 and K_2 are the viscosity and inertial coefficients respectively.

Experimental validation of the numerical methodology

This section presents the experimental validation of the numerical methodology explained in section 4.1 for case # 0 (Table 1). Also, the shape of the porous media (Fig. 3) and the different possible boundary conditions (Fig. 4) have been analysed to determine numerically which representative shape and boundary conditions are the most accurate in predicting the pressure drop.

The differential pressure per unit thickness of the OVR (ΔP/L), measured during the experiment, is depicted in Fig. 8 for stacks of 5, 10 and 15 meshes and with inlet air velocities ranging from 0 to 5 m/s. It is important to note that while the ΔP/L for the 10-mesh and 15-mesh stacks are essentially the same, the one of 5-mesh stack is lower. This

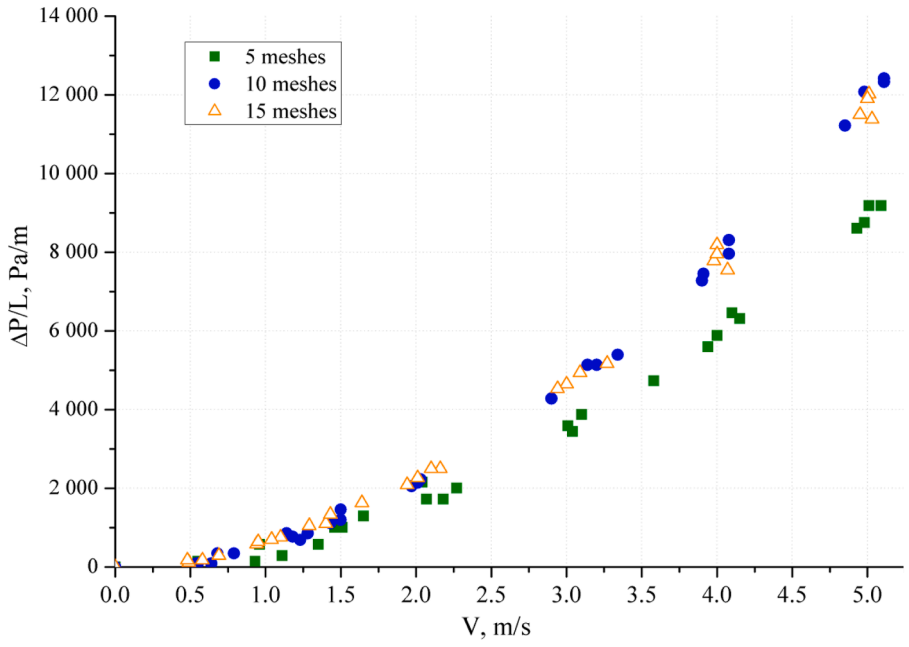


Fig. 8. Experimental differential pressure per unit thickness of the porous media for stacks of 5, 10 and 15 meshes.

lower ΔP/L for the 5-mesh stack is a consequence of the value of the compactness factor, c_f. For the 5-mesh stack, the c_f takes a value of 0.7 whereas for the 10-mesh and 15-mesh stacks, the c_f values are 0.59 and 0.58 respectively. In this case, with an inlet air velocity of 5 m/s, the ΔP/L for the 5-mesh stack is ~9 kPa/m, ~12 kPa/m for the 10-mesh stack and ~11.7 kPa/m for the 15-mesh stack. These values present the effect of the compactness factor in the ΔP/L, which is taken into account for the development of the CFD geometries made with similar compactness factor values to those of the 10-mesh and 15-mesh stacks (Table 1). It is worth noting that ΔP/L is no long dependent on the thickness of the stack in the experimental range of the 10 and 15 meshes stacks due to the fully developed flow. For the 5-mesh stack, it is difficult to conclude the same because of the less accurate hand-made process. Given these experimental results, it was decided to carry out and report results of numerical simulations with only stacks of 10 meshes as it required less computational time than the 15-mesh stack. In addition, the literature indicates that the optimal number of meshes in a dense wire mesh volumetric absorber for CST technology is between 10 and 15 [5].

Fig. 9 shows the experimental values of ΔP/L for the stack of 10 meshes and the CFD results from the four arrangements presented in Table 3 (A1, A2, A3, A4), which take into consideration the two different boundary conditions (Fig. 4) and two shapes of the porous media (Fig. 5). As depicted, at the highest velocity, 5 m/s, arrangements 1 (A1) and 2 (A2) diverge from the experimental results whereas

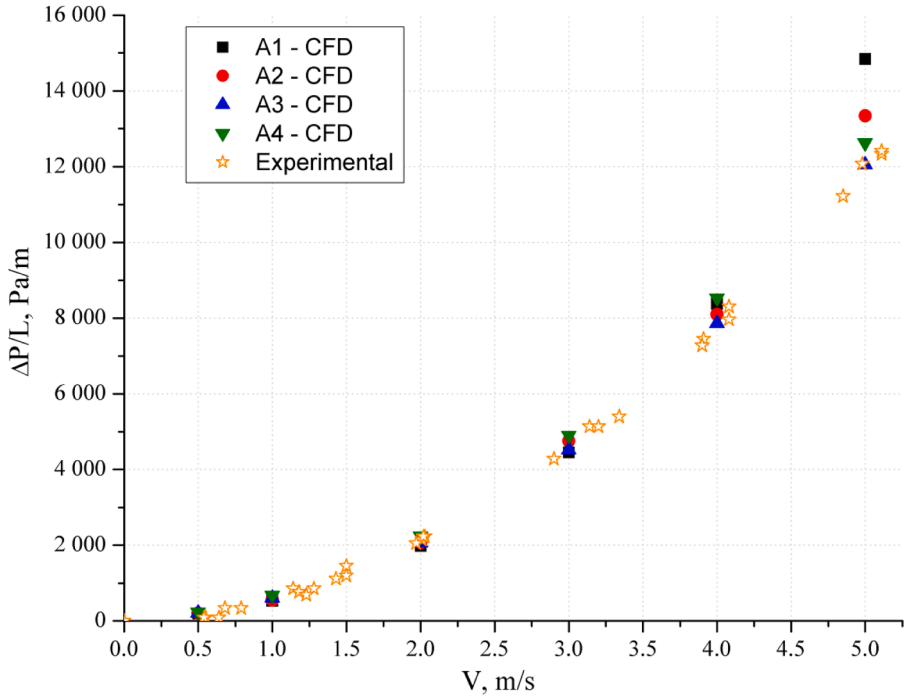


Fig. 9. Comparison of the ΔP/L between CFD arrangements and experimental test results.

arrangements 3 (A3) and 4 (A4) have similar ΔP/L CFD results. At lower velocities, all the arrangements have similar values, even though, arrangement 3 has the lowest deviation.

In addition, Table 4 compares the differential pressure per unit length obtained with the experimental test of 10 meshes with the ΔP/L CFD results obtained for the four arrangements for three inlet velocities: 1, 3 and 5 m/s. Moreover, Table 4 presents the deviations in the ΔP/L of each arrangement with respect to the experimental test of 10 meshes for each inlet air velocity and the average deviation. As can be seen in each arrangement, A1 and A2 diverge at low and high velocities from the experimental test results. A4 diverges the most at low velocities, and at high velocities has values similar to those of the experimental test. A3 is the best arrangement with results that are closest to those of the experimental test of the 10-mesh stack. The rectangular shape (A1 and A2) cannot be considered in the study any longer because of their deviations, although A4 has even higher deviation than the rectangular stacks.

Consequently, Fig. 10 shows a detailed analysis of the boundary conditions studied through a comparison of the experimental and numerical results for arrangements A3 and A4 and the deviation of the numerical results from the experimental ones. Taking the experimental results as a reference, e.g., at an inlet air velocity of 4 m/s, the deviation of the CFD ΔP/L for arrangement A3 is 0.9%, while for arrangement A4 has a deviation of 9.5%. Furthermore, the maximum deviation of arrangement A3 has a value of 8.1% at the lowest air velocity while arrangement A4 has a deviation of 23.2% at the same inlet air velocity. Finally, for the range of inlet air velocities analysed, the average deviation for the CFD ΔP/L results in arrangement A3 is 2.2% and 10.7% for arrangement A4, showing the importance of analysing the lateral boundaries and the shape.

Based on the results presented in this section, arrangement A3, which corresponds to a circular geometry (G2) with a symmetry plane as the lateral boundary (

Table 3), is the one that matches the experimental results and validates the numerical methodology proposed in this work best. In addition, Eq. (8) and Eq. (9) presents the coefficients K_1 and K_2 that fit Eq. (7) for the experimental results and arrangement 3 (A3).

$$\left(-\frac{dp}{dz}\right)_{experimental} = \frac{\mu}{1.13\cdot10^{-7}}V + \frac{\rho}{2.64\cdot10^{-3}}V^2 \tag{8}$$

$$\left(-\frac{dp}{dz}\right)_{A3} = \frac{\mu}{1.27\cdot10^{-7}}V + \frac{\rho}{2.60\cdot10^{-3}}V^2 \tag{9}$$

Taking the experimental correlation for the 10-mesh stack as reference (Eq. (8)), two comparisons are made with arrangement 3. First, the comparison between the results obtained from the CFD ΔP/L for A3 and the experimental correlation (Eq. (8)). This comparison is presented in Table 4, in which the average deviation between the CFD results for the arrangement 3 and the experimental correlation is 2.2%.

Second, the comparison between the numerical correlation (Eq. (9)) for A3 and the experimental correlation (Eq. (8)).

Table 5 presents the pressure drop results obtained with the CFD results for A3 and the numerical correlation for A3, both compared to the experimental correlation (Eq. (8)). As can be seen, the A3 correlation fits the experimental correlation better, with an average deviation of 1.2%, whereas the results of the A3 CFD ΔP/L compared to the experimental correlation have an average deviation of 2.2%. As a consequence, both comparisons result in the validation of the A3 CFD model (shape and boundary conditions) and for that reason it is used in the following section 5.2.

Effect of geometrical parameters for a single porosity mesh on pressure drop

With the numerical methodology to infer the differential pressure across the porous structure having been validated, this section analyses the ΔP/L for a wire mesh stack with a single screen porosity of 80% (∅), for three different wire diameters (0.1 mm, 0.4 mm and 0.7 mm) with a staggered stack pattern, having the main properties presented in Table 1. After that, individual correlations for each case studied are presented and finally, a generalised correlation for all the cases is developed.

Parametric analysis and individual correlations

To perform the parametric analysis for the three wire diameters (0.1 mm, 0.4 mm and 0.7 mm), the numerical methodology explained in section 4.1 was implemented. This numerical methodology is based on dense wire meshes with a circular shape (G2) as a representative geometry (Fig. 3) and a symmetry plane boundary as lateral walls (Fig. 4) as has been validated in section 5.1. The three detailed geometries (case # 1, case # 2 and case # 3 in Table 1) were created with the CAD module in the STAR-CCM+ software, all meshes having the same individual screen porosity, 80%. After that, a grid sensitivity analysis was performed in order to obtain the best grid possible for each geometry to produce accurate results (Appendix 1).

Table 6 shows the number of cells for the three geometries used in this section. Once the geometries and the grids were prepared, a sensitivity analysis of the air velocity at the absorber inlet surface was done, for each one of the three geometries (case # 1, case # 2 and case # 3). As a result, Fig. 11 depicts the pressure drop per porous thickness at all inlet velocities for the cases of 0.7 mm wire diameter (case # 1), 0.4 mm wire diameter (case # 2) and 0.1 mm wire diameter (case # 3). The differences between the three cases are easily observable in Fig. 11, which shows that the smaller the wire diameter and the larger the specific surface area (Table 1), the greater the pressure drop through the porous structure. Further comparison is shown for a velocity of 5 m/s, with case # 1 having a ΔP/L of 30 kPa/m, case # 2 having a value of 57 kPa/m and case # 3 having a value of 397 kPa/m, which means that for the structures with the same porosity the differential pressure could be increased up to 13 times depending on the wire diameter.

The scatter data presented in Fig. 11 is used to determine individual correlations (dashed lines in Fig. 11) that follow Eq. (7) for each one of the cases studied.

Table 7 presents the values K_1 and K_2 together with the average and the maximum deviations. It is worth noting that the average deviation of all the individual correlations is below 3% and that the maximum deviation is for case # 2, which is lower than 10%.

Table 4
Comparison of the experimental ΔP/L for a 10-mesh stack with the CFD ΔP/L values of the four arrangements analysed.

V m/s	Exp. test (10 meshes)	CFD							
		A1		A2		A3		A4	
	ΔP/L Pa/m	ΔP/L Pa/m	Dev. %	ΔP/L Pa/m	Dev. %	ΔP/L Pa/m	Dev. %	ΔP/L Pa/m	Dev. %
1	609.4	531.3	12.8	553.3	9.2	603.6	0.9	675.9	10.9
3	4,504.5	4,448.6	1.2	4,755.4	5.6	4,527.5	0.5	4,897.2	8.7
5	11,968.0	14,842.1	24.0	13,346.5	11.5	12,049.1	0.7	12,626.2	5.5
Average Deviation, %		8.9		6.6		2.2		10.7	

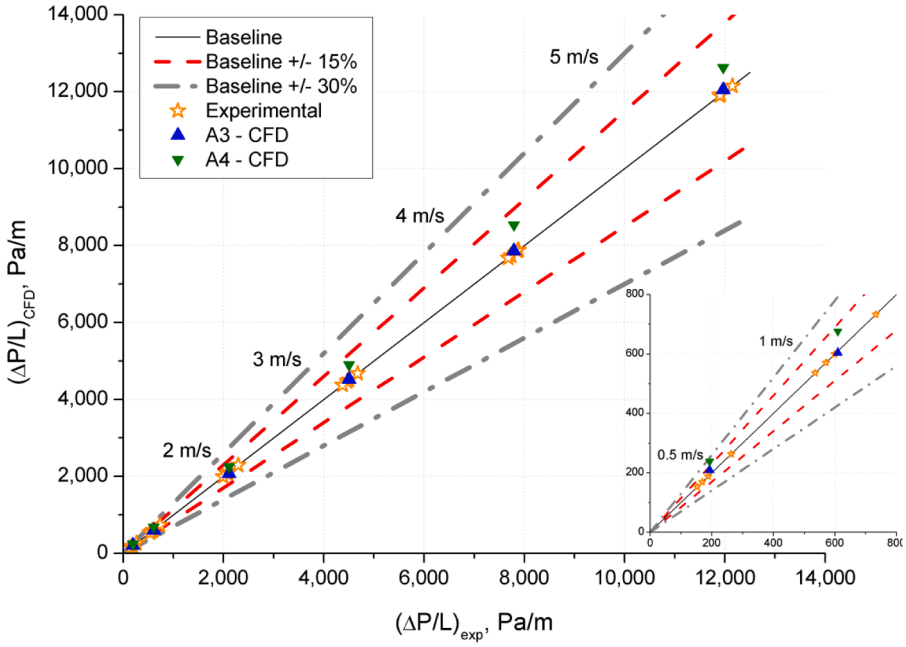


Fig. 10. Deviation of the A3 and A4 CFD ΔP/Ls with respect the experimental results.

Table 5
Comparison of the experimental ΔP/L for a 10-mesh stack with the ΔP/L results from the numerical correlation for the A3 and with the CFD ΔP/L values of the A3.

V m/s	Exp. test (10 meshes)	A3 correlation		A3 CFD	
	ΔP/L Pa/m	ΔP/L Pa/m	Dev. %	ΔP/L Pa/m	Dev. %
0.5	193.2	186.3	3.6	208.9	8.1
1	609.4	599.2	1.7	603.6	0.9
2	2,110.9	2,105.0	0.3	2,068.0	2.0
3	4,504.5	4,517.3	0.3	4,527.5	0.5
4	7,790.2	7,836.3	0.6	7,859.4	0.9
5	11,968.0	12,061.9	0.8	12,049.1	0.7
Average Deviation, %		1.2		2.2	

Table 6
Geometrical properties and parameters of the volumetric absorbers studied with 80% individual screen mesh porosity.

Case	d, mm	M, mm^{-1}	Geometry	Lateral surface	Number of Cells
# 1	0.7	0.35	2	Symmetry Plane	8,416,348
# 2	0.4	0.61	2	Symmetry Plane	8,397,076
# 3	0.1	2.44	2	Symmetry Plane	9,782,081

Generalised pressure drop correlation

This section covers the geometrical parameters influence in the pressure drop, presenting a generalised correlation based on those parameters for a fixed porosity and a wire diameter range. As mentioned in the introduction, there is a lack of information about the effect of the geometrical parameters (M or d) of stacked wire meshes in predicting the pressure drop for concentrated solar tower applications. Section 5.2.1 presents the individual correlations for each one of the cases analysed; however, generalised correlations are even more useful in performing optimisation and sensitivity studies in the solar field [39, 47–54].

Darcy's law with the Forchheimer extension, presented in equation (7), is not able to correlate the geometrical parameters with the pressure drop across the porous media. So, to obtain a general correlation of the pressure drop as a function of the geometrical parameters (M or d) for a single mesh porosity of 80%, the Ergun equation is adopted, which is an accurate model for an incompressible fluid and a steady flow for rigid and homogenous porous medium [29,46]. The Ergun equation is defined by the following expression [55]:

$$\frac{dp}{dz} = \frac{\alpha \cdot a_v^2 \cdot (1-\varnothing)^2 \cdot \mu \cdot V}{\varnothing^3} + \frac{\beta \cdot a_v \cdot (1-\varnothing) \cdot \rho \cdot V^2}{\varnothing^2} \tag{10}$$

Where α and β are empirical correction factors, a_v is the specific surface area, ∅ is the porosity of the porous, μ and ρ are the dynamic viscosity and the density of the fluid.

In order to present a generalised correlation for a single mesh porosity of 80% in a staggered stack, equation (2) is substituted into equation (10), to produce a new correlation:

$$dp/dz = \alpha \cdot f_1 \cdot M^2 \cdot \mu \cdot V + \beta \cdot f_2 \cdot M \cdot \rho \cdot V^2 \tag{11}$$

In Eq. (11), terms f_1 and f_2, depend on the porosity, ∅, which is 0.8 in this study, as well as the dimensionless constant expression a_v/M, having the following form:

$$f_1 = \frac{\left(\frac{a_v}{M}\right)^2 \cdot (1-\varnothing)^2}{\varnothing^3} \tag{12}$$

$$f_2 = \frac{\frac{a_v}{M} \cdot (1-\varnothing)}{\varnothing^2} \tag{13}$$

Moreover, α and β are two dimensionless empirical factors dependent on the porosity which have been numerically determined using the MATLAB fitting tool. The resulting equation for the general correlation is:

$$dp/dz = 425.04 \cdot M^2 \cdot \mu \cdot V + 2.292 \cdot M \cdot \rho \cdot V^2 \tag{14}$$

The generalised correlation is valid for forced air flow through staggered stack dense wire meshes with a single mesh porosity of 0.8, a wire diameter ranging from 0.1 to 0.7 mm and an air inlet velocity ranging from 0.5 to 5 m/s.

In this work, the generalised correlation adopted is defined by Eq. (14), and it is adapted from Eq. (10). This new correlation has a better

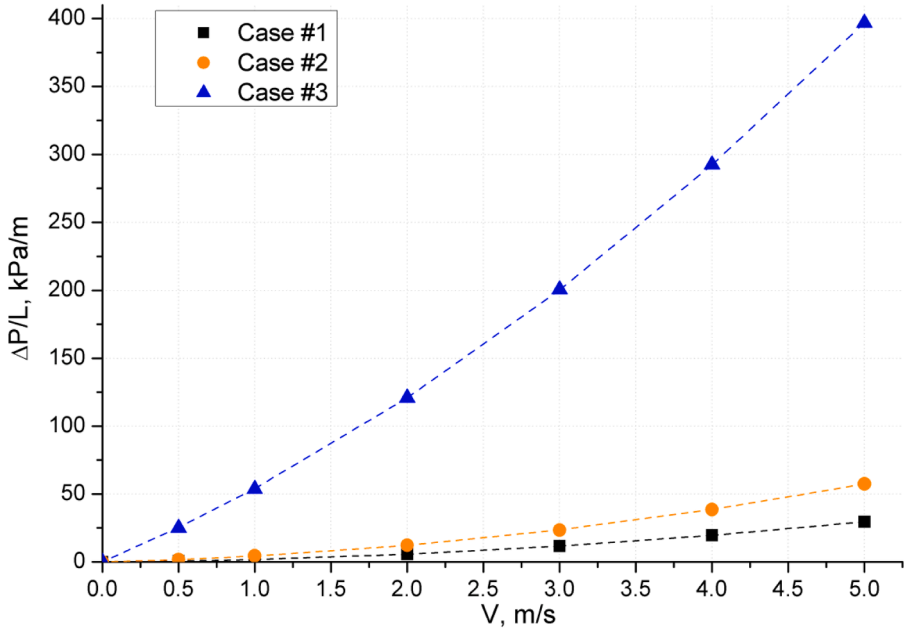


Fig. 11. CFD pressure drop through the porous thickness for case # 1, case # 2 and case # 3 at all inlet air velocities (scatter plot) and individual correlations (dash line plot).

Table 7
Differential pressure correlations for each case and the related deviations.

Case	K_1, m^2	K_2, m	Average deviation, %	Maximum deviation, %
# 1	2.21E-08	1.16E-03	1.0	4.4
# 2	7.35E-09	6.57E-04	2.6	8.5
# 3	3.87E-10	1.86E-04	0.5	2.0

implementation to optimise a volumetric receiver. The reason is that, in Eq. (14), the terms α, β, f_1 and f_2 are constant and dimensionless for a fixed single mesh porosity. While in Eq. (10) the terms α, β, f_1 and f_2 must be calculated for each wire diameter regardless the fixed porosity. Moreover, f_1 ($f_1=(a_v^2\cdot(1-\varnothing)^2)/\varnothing^3$) and f_2 ($f_2=(a_v\cdot(1-\varnothing))/\varnothing^2$) are not dimensionless in Eq. (10).

In order to analyse the agreement between the generalised correlation (GC)(Eq. (14)), the coefficients of the individual correlations (IC) (Table 7) and the numerical CFD results shown in Fig. 11, Table 8 presents the main ΔP/L results for two extreme velocities, 0.5 and 5 m/s, for the three cases (# 1, # 2 and # 3) studied in this work. At the lowest velocity modelled, 0.5 m/s, the generalised correlation comes closer to the CFD results than the individual correlations. However, at the highest velocity modelled, the individual correlations match the CFD results more closely.

For the shake of clarity,

Table 9 depicts the deviation between the different results, showing that at the lowest velocity (0.5 m/s) the GC has an absolute and maximum deviation with respect the CFD numerical results of 2%, while the maximum deviation of the IC reaches a value of 8.6%. Conversely at the highest velocity (5 m/s), the maximum deviation between the GC and the CFD numerical results is 4.1% while the maximum deviation between the IC and the CFD results is only 0.2%.

Finally, the mean and the maximum deviations of the individual and the generalised correlations with respect to the CFD results for each case are shown in

Table 10. As the average and the maximum deviations for all the correlations, GC and IC, are below 3 and 10% respectively, all the correlations can be considered valid for predicting the pressure drop in staggered stack dense wire meshes.

Conclusions

This research has two main objectives: the development and validation of a numerical methodology for predicting the pressure drop along dense wire meshes with a staggered arrangement, and the development of individual correlations for specific wire diameters (here, 0.7 mm, 0.4 mm and 0.1 mm) and a generalised correlation.

The main conclusions related to the first objective are:

Table 9
Deviation between CFD simulations, individual correlations, and generalised correlation for two extreme velocities modelled and three cases (#1, #2, #3).

V m/s	Case #1		Case #2		Case #3	
	D_{CFD-IC} %	D_{CFD-GC} %	D_{CFD-IC} %	D_{CFD-GC} %	D_{CFD-IC} %	D_{CFD-GC} %
0.5	4.4	-2.0	8.5	-0.5	-2.0	-0.3
5	-0.1	4.1	0.2	3.0	-0.1	-0.4

Table 8
Numerical ΔP/L results with CFD simulations, individual correlations, and generalised correlation for two extreme velocities and three cases (#1, #2, #3).

V m/s	Case #1			Case #2			Case #3		
	CFD kPa/m	IC kPa/m	GC kPa/m	CFD kPa/m	IC kPa/m	GC kPa/m	CFD kPa/m	IC kPa/m	GC kPa/m
0.5	0.70	0.67	0.72	1.86	1.70	1.87	24.96	25.46	25.02
5	29.6	29.6	28.4	57.5	57.3	55.8	396.8	397.1	398.3

Table 10
Average and maximum deviation between CFD simulations, individual correlations, and generalised correlation for the three cases (#1, #2, #3).

	Case #1		Case #2		Case #3	
	$D_{CFD\text{-}IC}$ %	$D_{CFD\text{-}GC}$ %	$D_{CFD\text{-}IC}$ %	$D_{CFD\text{-}GC}$ %	$D_{CFD\text{-}IC}$ %	$D_{CFD\text{-}GC}$ %
Average	1.0	2.5	2.6	1.3	0.5	0.4
Maximum	4.4	4.1	8.5	3.0	2.0	0.9

- Arrangement 3 (A3) was the best CFD model for estimating pressure drop. The assumptions implemented in A3 are a circular-shaped absorber, similar to the real experimental testing absorbers, with a symmetry plane as a lateral wall boundary.
- The numerical results of the arrangement 3 (A3) are fitted best by the permeability coefficients $K_1 = 1.27{\cdot}10^{-7}$ m^2 and $K_2 = 2.60{\cdot}10^{-3}$ m to infer the pressure drop with Darcy's law with the Forchheimer extension.
- The A3 correlation presents a maximum and an average deviation of 3.6% and 1.2% respectively, compared to the experimental correlation values.

With regard to the second objective, the study presents three individual correlations following Darcy's law with the Forchheimer extension and a generalised correlation based on the Ergun equation for wire diameters ranging from 0.1 to 0.7 mm with a 80% constant porosity, and concludes that:

- Individual correlations (IC) have maximum deviations up to 8.5% at the lowest air velocity, with average deviations up to 2.6%.
- The generalised correlation (GC) presents a maximum deviation up to 4.1% at the highest air velocity, and, the average deviations are up to 2.5%.
- All the correlations, IC and GC, can be used with great accuracy for dense wire meshes with a staggered stack pattern.

For future work the development of 85 and 90% porosity generalised correlations will be presented, as well as a possible meta-correlation for dense wire mesh absorbers from 80 to 90% porosity and wire diameters ranging from 0.1 to 0.7 mm. Furthermore, the effect of c_f in all the thermodynamic parameters is a new variable which needs study.

CRediT authorship contribution statement

Daniel Sanchez-Señoran: Data curation, Investigation, Methodology, Resources, Software, Validation, Visualization, Writing – original draft, Writing – review & editing. **Miguel A. Reyes-Belmonte:** Formal analysis, Investigation, Resources, Writing – review & editing. **Meryem Farchado:** Formal analysis, Investigation, Writing – review & editing. **Antonio L. Avila-Marin:** Conceptualization, Formal analysis, Funding acquisition, Investigation, Methodology, Project administration, Resources, Software, Supervision, Visualization, Writing – original draft, Writing – review & editing.

Declaration of competing interest

The authors declare that they have no known competing financial interests or personal relationships that could have appeared to influence the work reported in this paper.

Data availability

Data will be made available on request.

Acknowledgement

This work is part of the R&D Project INTECSOL, PID2021-126664OB-I00, funded by MCIN/AEI/10.13039/501100011033 and by the European Regional Development funding. This work was partially supported by the computing facilities of Extremadura Research Centre for Advanced Technologies (CETA-CIEMAT), funded by the European Regional Development Fund (ERDF). CETA-CIEMAT belongs to CIEMAT and the Government of Spain.

Appendix 1

A sensitivity grid analysis has been performed for all the cases in this work. Table A.1. shows the sensitivity grid for case #2. The adopted base size is 0.5 mm with a deviation of 1.5% with respect to the best base size analysed of 0.3 mm. The analysis is done for the highest air velocity, 5 m/s.

For case #1, the comparison is between the selected base size, 0.875 mm, and the best base size analysed, 0.6 mm resulting in 14,936,501 cells. The deviation is 2.2% and the pressure drop for 5 m/s is 249.4 and 244.1 Pa respectively.

The base size selected for case #3 is 0.125 mm with a deviation of 1.3% from the best base size analysed, 0.09 mm (16,252,414 cells). The pressure drop presented in both base sizes is 483.0 and 489.1 Pa respectively at 5 m/s of inlet velocity.

Appendix 2

The original thermal anemometer (TA1) has been checked with another (TA2) of the same model with the same attributes.

The original differential pressure meter (ΔP1) used in the experimental setup works in a range between 0 and 130 mbar. However, the differential pressure meter used to double-check the results works in a range between 0 and 1 bar (ΔP2).

Fig. A.1. presents, for a random porous sample, the check performed using the main gauges. Concerning the differential pressure measurements, meter 2 (ΔP2) can be seen not to be accurate enough for the experimental measures carried out in this work, as it has a lower resolution than ΔP1 in the range measured. However, at velocities higher than 2 m/s, ΔP2 is able to replicate the trend curve of ΔP1, which has better resolution for these porous samples. Regarding the thermal anemometer (TA), both are the same model and have the same accuracy and range giving similar values for the same operating conditions. So, based on these results, ΔP1 and TA1 were selected as the main measuring devices for this work.

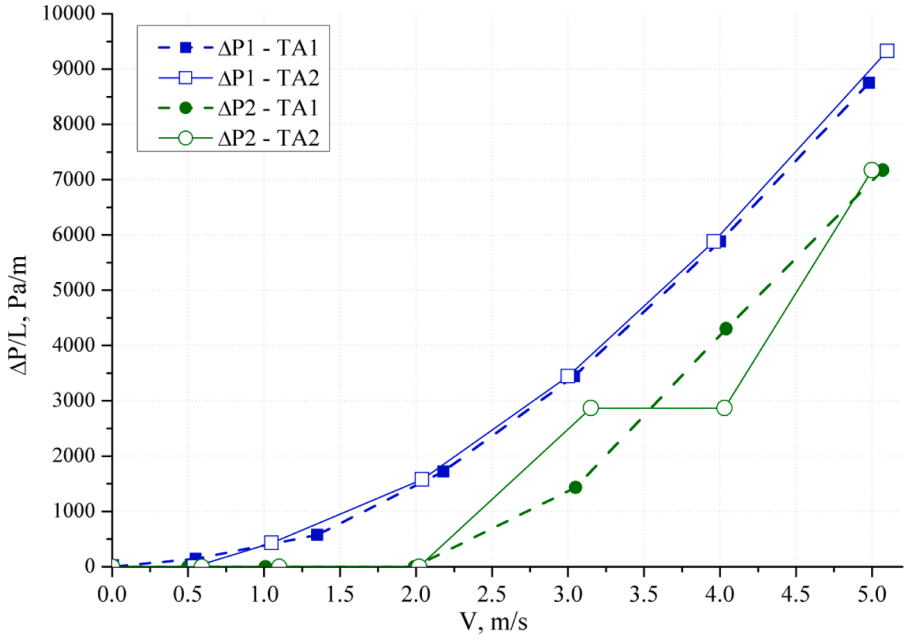


Fig. A.1. Comparisons used to select the equipment for the experimental setup.

Table A.1
Sensitivity grid analysis for case #2. Pressure drop at 5 m/s and deviations for each base size.

Base Size, mm	Number of cells	Pressure Drop for 5 m/s, Pa	Deviation, %
2	513,712	284.4	3.5
1	1,862,142	281.8	2.6
0.5	8,397,076	278.7	1.5
0.4	11,243,701	276.1	0.5
0.3	19,118,286	274.7	-

References

[1] A.L. Avila-Marin, J. Fernandez-Reche, S. Gianella, L. Ferrari, D. Sanchez-Señoran, Experimental study of innovative periodic cellular structures as air volumetric absorbers, Renew. Energy 184 (2022) 391–404, https://doi.org/10.1016/j.renene.2021.11.021.

[2] C. Pabst, G. Feckler, S. Schmitz, O. Smirnova, R. Capuano, P. Hirth, T. Fend, Experimental performance of an advanced metal volumetric air receiver for Solar Towers, Renew. Energy 106 (2017) 91–98, https://doi.org/10.1016/j.renene.2017.01.016.

[3] R.T. Broeske, P. Schwarzbözl, B. Hoffschmidt, A new partitioned 1D LTNE continuum model for the simulation of 3D-shaped honeycomb absorbers, Sol. Energy 236 (2022) 533–547, https://doi.org/10.1016/j.solener.2022.02.024.

[4] L. Savoldi, A. Allio, A. Bonvento, M. Cantone, J. Fernandez Reche, Experimental and numerical investigation of a porous receiver equipped with Raschig Rings for CSP applications, Sol. Energy 212 (2020) 309–325, https://doi.org/10.1016/j.solener.2020.11.006.

[5] A.L. Avila-Marin, M. Alvarez de Lara, J. Fernandez-Reche, Experimental results of gradual porosity volumetric air receivers with wire meshes, Renew. Energy 122 (2018) 339–353, https://doi.org/10.1016/j.renene.2018.01.073.

[6] X. Rández, F. Zaversky, D. Astrain, A novel active volumetric rotating disks solar receiver for concentrated solar power generation, Appl. Therm. Eng. 206 (2022) 118114, https://doi.org/10.1016/j.applthermaleng.2022.118114.

[7] F. Gomez-Garcia, J. González-Aguilar, G. Olalde, M. Romero, Thermal and hydrodynamic behavior of ceramic volumetric absorbers for central receiver solar power plants: A review, Renew. Sustain. Energy Rev. 57 (2016) 648–658, https://doi.org/10.1016/j.rser.2015.12.106.

[8] L.S. Tong, A.L. London, Heat-Transfer and Flow-Friction Characteristics of Woven-Screen and Crossed-Rod Matrixes, Trans. Am. Soc. Mech. Eng. 79 (1956) 1558–1570, https://doi.org/10.1115/1.4013401.

[9] A.L. London, J.W. Mitchell, W.A. Sutherland, Heat-Transfer and Flow-Friction Characteristics of Crossed-Rod Matrices, J. Heat Transf. 82 (1960) 199–213, https://doi.org/10.1115/1.3679911.

[10] G.S. Beavers, E.M. Sparrow, Non-Darcy Flow Through Fibrous Porous Media, J. Appl. Mech. 36 (1969) 711–714, https://doi.org/10.1115/1.3564760.

[11] P. Du Plessis, A. Montillet, J. Comiti, J. Legrand, Pressure drop prediction for flow through high porosity metallic foams, Chem. Eng. Sci. 49 (1994) 3545–3553, https://doi.org/10.1016/0009-2509(94)00170-7.

[12] A. Bhattacharya, V.V. Calmidi, R.L. Mahajan, Thermophysical properties of high porosity metal foams, Int. J. Heat Mass Transf. 45 (2002) 1017–1031, https://doi.org/10.1016/S0017-9310(01)00220-4.

[13] P. Khayargoli, V. Loya, L.-P. Lefebvre, M. Medraj, The impact of microstructure on the permeability of metal foams, 2004 (2004).

[14] L. Tadrist, M. Miscevic, O. Rahli, F. Topin, About the use of fibrous materials in compact heat exchangers, Exp. Therm. Fluid Sci. 28 (2004) 193–199, https://doi.org/10.1016/S0894-1777(03)00039-6.

[15] J.-P. Bonnet, F. Topin, L. Tadrist, Flow Laws in Metal Foams: Compressibility and Pore Size Effects, Transp. Porous Media 73 (2008) 233–254, https://doi.org/10.1007/s11242-007-9169-5.

[16] J.-H. Joo, B.-S. Kang, K.-J. Kang, Experimental Studies on Friction Factor and Heat Transfer Characteristics Through Wire-Woven Bulk Kagome Structure, Exp. Heat Transf. 22 (2009) 99–116, https://doi.org/10.1080/08916150902718591.

[17] A. Kołodziej, J. Łojewska, Experimental and modelling study on flow resistance of wire gauzes, Chem. Eng. Process. Process Intensif. 48 (2009) 816–822, https://doi.org/10.1016/j.cep.2008.10.009.

[18] R. Dyga, M. Płaczek, Efficiency of heat transfer in heat exchangers with wire mesh packing, Int. J. Heat Mass Transf. 53 (2010) 5499–5508, https://doi.org/10.1016/j.ijheatmasstransfer.2010.07.007.

[19] J. Ma, P. Lv, X. Luo, Y. Liu, H. Li, J. Wen, Experimental investigation of flow and heat transfer characteristics in double-laminated sintered woven wire mesh, Appl. Therm. Eng. 95 (2016) 53–61, https://doi.org/10.1016/j.applthermaleng.2015.11.015.

[20] R. Kurian, C. Balaji, S.P. Venkateshan, Experimental investigation of convective heat transfer in a vertical channel with brass wire mesh blocks, Int. J. Therm. Sci. 99 (2016) 170–179, https://doi.org/10.1016/j.ijthermalsci.2015.08.002.

[21] B. Kotresha, N. Gnanasekaran, Determination of interfacial heat transfer coefficient for the flow assisted mixed convection through brass wire mesh, Int. J. Therm. Sci. 138 (2019) 98–108, https://doi.org/10.1016/j.ijthermalsci.2018.12.043.

[22] J. Zhao, M. Sun, L. Zhang, C. Hu, D. Tang, L. Yang, Y. Song, Forced Convection Heat Transfer in Porous Structure: Effect of Morphology on Pressure Drop and Heat

Transfer Coefficient, J. Therm. Sci. 30 (2021) 363–393, https://doi.org/10.1007/s11630-021-1403-x.
[23] B. Thomas, D. Pittman, Update on the evaluation of different correlations for the flow friction factor and heat transfer of Stirling engine regenerators, Collect. Tech. Pap. 35th Intersoc. Energy Convers. Eng. Conf. Exhib. IECEC Cat No00CH37022 1 (2000) 76–84, https://doi.org/10.1109/IECEC.2000.870632, vol.
[24] M. Becker, Th. Fend, B. Hoffschmidt, R. Pitz-Paal, O. Reutter, V. Stamatov, M. Steven, D. Trimis, Theoretical and numerical investigation of flow stability in porous materials applied as volumetric solar receivers, Sol. Energy 80 (2006) 1241–1248, https://doi.org/10.1016/j.solener.2005.11.006.
[25] S.C. Costa, H. Barrutia, J.A. Esnaola, M. Tutar, Numerical study of the pressure drop phenomena in wound woven wire matrix of a Stirling regenerator, Energy Convers. Manag. 67 (2013) 57–65, https://doi.org/10.1016/j.enconman.2012.10.014.
[26] B.T. York, B.D. MacDonald, Influence of misalignment and spacing on the pressure drop through wire mesh Stirling engine regenerators, Energy Convers. Manag. 245 (2021) 114588, https://doi.org/10.1016/j.enconman.2021.114588.
[27] R.T. Broeske, P. Schwarzbözl, B. Hoffschmidt, Multi-dimensional numerical analysis of flow instabilities in 3D-shaped honeycomb absorbers, Sol. Energy 247 (2022) 86–95, https://doi.org/10.1016/j.solener.2022.10.007.
[28] A.L. Avila-Marin, J. Fernandez-Reche, M. Casanova, C. Caliot, G. Flamant, Numerical simulation of convective heat transfer for inline and stagger stacked plain-weave wire mesh screens and comparison with a local thermal non-equilibrium model, 2017. https://doi.org/10.1063/1.4984346.
[29] Z. Wu, C. Caliot, F. Bai, G. Flamant, Z. Wang, J. Zhang, C. Tian, Experimental and numerical studies of the pressure drop in ceramic foams for volumetric solar receiver applications, Appl. Energy 87 (2010) 504–513, https://doi.org/10.1016/j.apenergy.2009.08.009.
[30] Z. Wu, C. Caliot, G. Flamant, Z. Wang, Numerical simulation of convective heat transfer between air flow and ceramic foams to optimise volumetric solar air receiver performances, Int. J. Heat Mass Transf. 54 (2011) 1527–1537, https://doi.org/10.1016/j.ijheatmasstransfer.2010.11.037.
[31] A. Jafarizade, M. Panjepour, M. Meratian, M.Davazdah Emami, Numerical Simulation of Gas/Solid Heat Transfer in Metallic Foams: A General Correlation for Different Porosities and Pore Sizes, Transp. Porous Media 127 (2019) 481–506, https://doi.org/10.1007/s11242-018-1208-x.
[32] D. Sanchez-Señoran, M.A. Reyes-Belmonte, J. Fernandez-Reche, A.L. Avila-Marin, Numerical simulation of convective heat transfer coefficient in wire mesh absorbers with fixed porosity, Results Eng 17 (2023) 100830, https://doi.org/10.1016/j.rineng.2022.100830.
[33] D. Sanchez-Señoran, M.A. Reyes-Belmonte, J. Fernandez-Reche, A.L. Avila-Marin, Numerical simulation of convective heat transfer coefficient in wire mesh absorbers with 0.1mm wire diameter, AIP Conf. Proc. 2815 (2023) 100011, https://doi.org/10.1063/5.0148754.
[34] J. Xu, R.A. Wirtz, In-plane effective thermal conductivity of plain-weave screen laminates, IEEE Trans. Compon. Packag. Technol. 25 (2002) 615–620, https://doi.org/10.1109/TCAPT.2002.807993.
[35] J.-W. Park, D. Ruch, R. Wirtz, Thermal/fluid characteristics of isotropic plain-weave screen laminates as heat exchange surfaces. 40th AIAA Aerosp. Sci. Meet. Exhib, American Institute of Aeronautics and Astronautics, 2002, https://doi.org/10.2514/6.2002-208.
[36] Z. Zhao, Y. Peles, M.K. Jensen, Properties of plain weave metallic wire mesh screens, Int. J. Heat Mass Transf. 57 (2013) 690–697, https://doi.org/10.1016/j.ijheatmasstransfer.2012.10.055.
[37] A.L. Avila-Marin, C. Caliot, G. Flamant, M. Alvarez de Lara, J. Fernandez-Reche, Numerical determination of the heat transfer coefficient for volumetric air receivers with wire meshes, Sol. Energy 162 (2018) 317–329, https://doi.org/10.1016/j.solener.2018.01.034.
[38] A.L. Avila-Marin, C. Caliot, M. Alvarez de Lara, J. Fernandez-Reche, M.J. Montes, A. Martinez-Tarifa, Homogeneous equivalent model coupled with P1-approximation for dense wire meshes volumetric air receivers, Renew. Energy 135 (2019) 908–919, https://doi.org/10.1016/j.renene.2018.12.061.
[39] A.L. Avila-Marin, CFD parametric analysis of wire meshes open volumetric receivers with axial-varied porosity and comparison with small-scale solar receiver tests, Renew. Energy 193 (2022) 1094–1105, https://doi.org/10.1016/j.renene.2022.05.060.
[40] Daniel Sanchez-Señoran, Miguel A. Reyes-Belmonte, Jesus Fernandez-Reche, Antonio L. Avila-Marin, Numerical Simulation of Pressure Drop in Wire Mesh Absorbers with Fixed Porosity, Poster SolarPaces Conf (2022) 2022.
[41] R. Pitz-Paal, B. Hoffschmidt, M. Böhmer, M. Becker, Experimental and numerical evaluation of the performance and flow stability of different types of open volumetric absorbers under non-homogeneous irradiation, Sol. Energy 60 (1997) 135–150, https://doi.org/10.1016/S0038-092X(97)00007-8.
[42] C. Heisel, C. Caliot, T. Chartier, S. Chupin, P. David, D. Rochais, Digital design and 3D printing of innovative SiC architectures for high temperature volumetric solar receivers, Sol. Energy Mater. Sol. Cells 232 (2021) 111336, https://doi.org/10.1016/j.solmat.2021.111336.
[43] Siemens Digital Industries Software, User Guide - Simcenter STAR-CCM+ Documentation, SIEMENS, 2020.
[44] H.K. Versteeg, W. Malalasekera, An introduction to computational fluid dynamics. The finite volume method, Longman Scientific and Technical, 1995.
[45] Suhas V. Patankar, Numerical Heat Transfer and Fluid Flow, McGraw-Hill, 1980.
[46] N. Dukhan, P. Patel, Equivalent particle diameter and length scale for pressure drop in porous metals, Exp. Therm. Fluid Sci. 32 (2008) 1059–1067, https://doi.org/10.1016/j.expthermflusci.2007.12.001.
[47] Z. Wu, Z. Wang, Fully coupled transient modeling of ceramic foam volumetric solar air receiver, Sol. Energy 89 (2013) 122–133, https://doi.org/10.1016/j.solener.2012.12.016.
[48] Z. Wu, C. Caliot, G. Flamant, Z. Wang, Coupled radiation and flow modeling in ceramic foam volumetric solar air receivers, Sol. Energy 85 (2011) 2374–2385, https://doi.org/10.1016/j.solener.2011.06.030.
[49] X. Chen, X.-L. Xia, X.-L. Meng, X.-H. Dong, Thermal performance analysis on a volumetric solar receiver with double-layer ceramic foam, Energy Convers. Manag. 97 (2015) 282–289, https://doi.org/10.1016/j.enconman.2015.03.066.
[50] M. Cagnoli, L. Savoldi, R. Zanino, F. Zaversky, Coupled optical and CFD parametric analysis of an open volumetric air receiver of honeycomb type for central tower CSP plants, Sol. Energy 155 (2017) 523–536, https://doi.org/10.1016/j.solener.2017.06.038.
[51] X. Chen, X.-L. Xia, X.-W. Yan, C. Sun, Heat transfer analysis of a volumetric solar receiver with composite porous structure, Energy Convers. Manag. 136 (2017) 262–269, https://doi.org/10.1016/j.enconman.2017.01.018.
[52] S. Du, T. Xia, Y.-L. He, Z.-Y. Li, D. Li, X.-Q. Xie, Experiment and optimization study on the radial graded porous volumetric solar receiver matching non-uniform solar flux distribution, Appl. Energy 275 (2020) 115343, https://doi.org/10.1016/j.apenergy.2020.115343.
[53] A. Godini, S. Kheradmand, Optimization of volumetric solar receiver geometry and porous media specifications, Renew. Energy 172 (2021) 574–581, https://doi.org/10.1016/j.renene.2021.03.040.
[54] A.L. Avila-Marin, J. Fernandez-Reche, J.A. Carballo, M.E. Carra, S. Gianella, L. Ferrari, D. Sanchez-Señoran, CFD analysis of the performance impact of geometrical shape on volumetric absorbers in a standard cup, Renew. Energy 201 (2022) 256–272, https://doi.org/10.1016/j.renene.2022.10.032.
[55] S. Ergun, A.A. Orning, Fluid Flow through Randomly Packed Columns and Fluidized Beds, Ind. Eng. Chem. 41 (1949) 1179–1184, https://doi.org/10.1021/ie50474a011.